

# Learning in a Multifield Coherent Ising Machine

Daan de Bos and Marc Serra-Garcia

AMOLF

Science Park 104, 1098XG Amsterdam, The Netherlands

(Dated: February 18, 2025)

Physical information processors can learn from examples if they are modified according to an abstract parameter update equation, termed a learning rule. We introduce a physical model for self-learning that encodes the learning rule in the Hamiltonian of the system. The model consists of a network of multi-modal resonators. One of the modes is driven parametrically into a bi-stable regime, forming a coherent Ising machine (CIM)—that provides the long-term memory that stores learned responses (weights). The CIM is augmented with an additional spinor field that acts as short-term (activation) memory. We numerically demonstrate that, in the presence of suitable nonlinear interactions between the long-term memory Ising machine and the short-term memory auxiliary field, the system autonomously learns from examples.

Keywords: Physical computing, parametric oscillators, physical learning, tight-binding model

## INTRODUCTION

Physical computing [1]—computing based on novel and unconventional phenomena and information carriers, has achieved remarkable successes. Some examples are photonic image recognition [2, 3] and equation solving [4, 5]; the use of thermal noise for matrix inversion [6], to perform inference [7] and to sample probability distributions [8]; the application of condensed-matter ideas such as topology [9], symmetry [10] and parametric phenomena [11] for computing; and the use of mechanical information carriers for the realization of acoustic arithmetic operations [12], passive speech recognition [13], passive event counting [14], and to embody intelligent responses in soft robots [15]. In contrast, physical learning—the process by which a physical computer autonomously improves its performance at a task by updating its parameters according to feedback and examples—is still comparatively in its infancy. Remarkable steps have been taken with the discovery of learning rules [16–23]—that indicate how parameters should be updated to improve system performance in a given information processing task; and some of these learning rules have been demonstrated in table-top experiments [24–26]. However, a significant gap remains between learning rules—which are abstract parameter update equations, and physical systems—governed by a Hamiltonian, and its interaction with the environment in the form of fluctuations and dissipation.

In this letter, we introduce a material model—a tight-binding Hamiltonian—that learns autonomously from a set of examples (Fig. 1). The model harnesses thermal fluctuations to drive transitions between states, and uses symmetry-protected degeneracies to construct two copies of the system, as required by contrastive learning rules. The incorporation of degeneracy and noise as building blocks of a self-learning physical system illustrates how phenomena that are not traditionally used for computation—or that are even actively avoided—can be reclaimed in novel information processing paradigms.

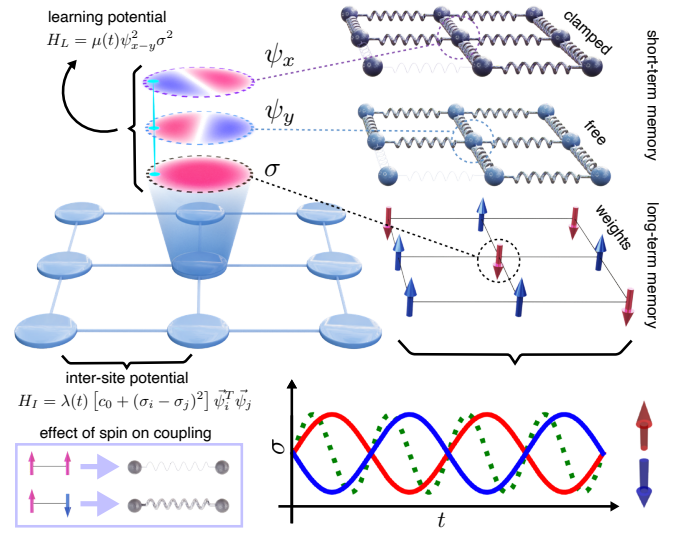


FIG. 1. A multifield coherent Ising machine is a network of multi-modal resonators, represented by a tight-binding model consisting of a scalar field  $\sigma$  interacting with a spinor field  $\vec{\psi}$ . At every site  $i$ , the model has three degrees of freedom  $\psi_{x,i}$ ,  $\psi_{y,i}$  and  $\sigma_i$ , coupled via the nonlinear terms  $H_L$  and  $H_I$ . The field  $\vec{\psi}$  corresponds to the computational degrees of freedom (neural activations).  $\vec{\psi}$  is composed of two identical sub-systems  $\psi_x$  and  $\psi_y$  (mass-spring lattices). During training, the output degree of freedom of the sub-system  $\psi_y$  is clamped to a target value ( $\psi_x$  is left free). The modes  $\sigma_i$  are parametrically pumped (dotted green line) into a bistable self-oscillation regime, modeled by a spin (up or down depending on the phase of oscillation). This results in an Ising-like system that provides a long-term memory and stores the learned weights. The nonlinear interaction term  $H_I$  modulates the dynamics of the computational field  $\vec{\psi}$  according to the weights  $\sigma$  (resulting in strong springs between antiferromagnetically-aligned sites). The term  $H_L$  causes the weights  $\sigma$  to be updated in response to a difference (contrast) between the free ( $\psi_x$ ) and clamped ( $\psi_y$ ) computational sub-systems. In a material, the field  $\vec{\psi}$  can be realized by mapping the two spin components to a pair of doubly-degenerate localized orbitals.

The proposed system, referred here as a *multifield coherent Ising machine* (Fig. 1), consists of a network of multi-modal resonators. Every site has three modes  $\sigma$ ,  $\psi_x$  and  $\psi_y$ . One of the modes, termed the long-term memory, learning or spin mode  $\sigma$ , is parametrically pumped into a bi-stable regime, forming a synthetic spin system known as a *coherent Ising machine* (CIM) [27, 28]. We use the bi-stability of the spin mode  $\sigma$  to store learned responses over long time scales, with the spin texture playing the role of the weights in a machine learning model. In addition to the spin field  $\sigma$ , two degenerate resonator modes are used to construct a synthetic spinor field  $\vec{\psi} = (\psi_x, \psi_y)$ . These modes will become the computational or short-term memory degrees of freedom—holding intermediate results of computations (neural activations). Nonlinear interactions between the modes, encoded in a learning Hamiltonian  $H_l$ , will cause the short-term dynamics of  $\vec{\psi}$  to be conditioned by the long-term memory  $\sigma$ —allowing the field  $\sigma$  to parameterize the computation.  $H_l$  will also cause the weights in  $\sigma$  to be updated according to a learning rule. A CIM interacting with an additional spinor field  $\vec{\psi}$  through a nonlinear term  $H_l$  is described by a Langevin equation:

$$\ddot{\vec{\psi}}_i + \frac{\omega_c}{Q_c} \dot{\vec{\psi}}_i + \omega_c^2 \vec{\psi}_i + \nabla_{\vec{\psi}_i} H_l = \vec{\xi}_{\psi,i}; \quad (1)$$

$$\ddot{\sigma}_i + \frac{\omega_l}{Q_l} \dot{\sigma}_i + \omega_l^2 (1 + \alpha \sin(2\omega_l t)) \sigma_i + \epsilon \sigma_i^3 + \nabla_{\sigma_i} H_l = \xi_{\sigma,i}. \quad (2)$$

Where  $i$  is the site number. We set the frequency of the computational and learning degrees of freedom to  $\omega_c^2 = 0.5$  and  $\omega_l^2 = 1$  respectively. The corresponding quality factors are set to  $Q_c = 4000$  and  $Q_l = 40$ , while the pumping strength is set to  $\alpha_l = 0.1$  and the Duffing coefficient is set to  $\epsilon = 0.005$ . The terms  $\xi$  correspond to uncorrelated (diagonal), Gaussian distributed thermal noise with an autocorrelation  $\langle \xi_{l/c}(t_0) \xi_{l/c}(t_1) \rangle = \sqrt{2k_B T b_{c/l}} \delta(t_1 - t_0)$ . Interactions between degrees of freedom are captured by the learning potential  $H_l = H_I + H_L$ , where the local part  $H_L$  couples the fields locally at every site of the lattice—updating the long-term memory according to the learning rule—and the interaction part  $H_I$  couples each site with its nearest neighbors—ensuring that information is processed according to the weights stored in the  $\sigma$  field.

The learning Hamiltonian  $H_l$  is designed by analogy to the contrastive learning rule [24], which involves comparing two copies of a system. We refer to these copies as *free* and *clamped* sub-systems. Both copies are presented with an excitation (in this work, a harmonic force at the resonance frequency  $\omega_c$  of the computational modes  $\psi_{x/y}$ ), at one or several input sites. The amplitude of this force encodes the input values. The output is obtained by reading the amplitude of oscillation of an output site. During learning, the output site of the clamped sub-system is forced to take a specific vibration amplitude. Then, the parameters (springs) are updated proportionally to the

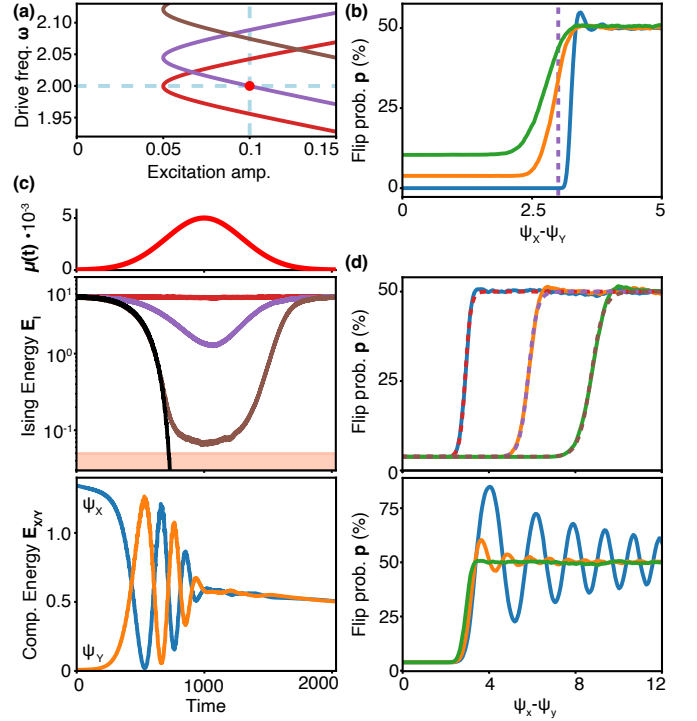


FIG. 2. Single-site learning dynamics. **(a)** Parametric self-oscillation regions corresponding to the contrast  $\psi_x - \psi_y$  values of 0 (red), 3 (purple) and 5 (brown). These contrasts are the left limit, dashed vertical line and right limit in panel (b). The red dot corresponds to the excitation parameters (frequency of  $2\omega_l = 2$  and amplitude of  $\omega_l^2 \alpha = 0.1$ ) (b). **(b)** Probability of flip during a learning protocol as a function of the contrast  $\psi_x - \psi_y$  for  $k_B T$  values of 0.001 (blue), 0.05 (orange) and 0.1 (green). **(c)** Transient dynamics during a learning protocol of width  $\Delta_T = 300$ . The top panel shows the interaction strength  $\mu(t)$  during the protocol. The middle panel shows the energy in the Ising mode  $\sigma$  (denoted  $E_I$ ), corresponding to a contrast of 0 (red), 3 (purple) and 5 (brown), with a temperature  $k_B T = 0.05$ . The black curve corresponds to a contrast of 5 but setting  $K_B T = 0.05$ . The bottom panel shows the Rabi oscillations in the energy  $E_X$  of the free ( $\psi_x$ ) mode, and the energy  $E_Y$  of the clamped ( $\psi_y$ ) mode, during the learning pulse. **(d)** Probability of spin flip as a function of the contrast  $\psi_x - \psi_y$ , for learning potentials  $\mu_m = \mu_{m,0}/n^2$  with  $n = 1$  (blue),  $n = 2$  (orange) and  $n = 3$  (green) [top] and of protocol durations  $\Delta_t = 50$  (blue),  $\Delta_t = 100$  (orange), and  $\Delta_t = 300$  (green) [bottom]. The dashed lines in the top panel shows the sigmoidal fit of Eq. 4. Throughout the figure,  $\mu_{m,0} = 0.005$ .

difference between the clamped and free energies. Although it can be proven that contrastive learning approximates gradient descent, intuitively, the learning rule can be understood as the changing the model parameters until the free system behaves like the clamped one—thus learning to produce the desired output.

The need for two system copies poses a practical challenge for implementing contrastive learning rules. In our realization, we address this by mapping each copy to a component of the spinor field  $\vec{\psi}$ , with  $\psi_x$  and  $\psi_y$  becoming the free and clamped copies respectively. Al-

though our work concerns a tight-binding model, in an actual condensed matter system, the two identical copies of the system can be robustly realized by associating them with basis functions that transform under a two-dimensional irreducible representation of the system's symmetry group, mapping each copy  $\psi_x$  and  $\psi_y$  to an irreducible symmetry sector [29]. In contrastive learning, spins are updated in response to a difference between forces in the clamped and free configurations. Here, we implement a variation of the learning rule where the long-term memory is updated (spins are flipped) in response to the clamped and free site oscillation amplitudes. Although our learning rule deviates significantly from traditional contrastive learning, as spins can only take discrete states and experience probabilistic updates, a similar intuition as with contrastive learning can be applied: spins will flip until the free copy—which does not have access to the target output—learns to naturally approximate the target values. This intuition will be validated numerically in the next sections.

### SINGLE-SITE LEARNING DYNAMICS

Our learning rule boils down to a conditional spin forgetting mechanism: the phase of a spin  $\sigma_i$  is randomized with a probability conditional on the difference between the clamped and free configurations at the site, thereby inducing spin flips in sites where free and clamped are misaligned. This mechanism arises from the following nonlinear, local interaction term acting on each site  $i$ ,

$$H_{L,i} = \mu(t) (\psi_{x,i} - \psi_{y,i})^2 \sigma_i^2 = \mu(t) \psi_{x-y,i}^2 \sigma_i^2. \quad (3)$$

Since  $\psi_x$  and  $\psi_y$  are degenerate modes, the contrast between clamped and free configurations  $\psi_{x-y}$  is merely a rotation of the local basis  $(\psi_{x+y}, \psi_{x-y}) = (\hat{\sigma}_x + \hat{\sigma}_z)(\psi_x, \psi_y)$ , where  $\hat{\sigma}_{x/y/z}$  is the corresponding Pauli matrix. This allows us to interpret  $H_L$  as a cross-Kerr interaction between the Ising field  $\sigma$  and the rotated computational field  $\psi_{x-y}$ . Thus, the term introduces a change in the resonance frequency of the mode  $\sigma_i$  that increases quadratically with the contrast  $\psi_{x-y} = \psi_x - \psi_y$  between clamped and free configurations. If  $\psi_{x-y}$  is sufficiently large, the system will be detuned outside the parametric resonance region (Fig. 2a), causing its oscillation to decay, thereby forgetting its state (Fig. 2b,c). At low temperatures, the detuning results in a sharp, step-like transition: If  $\psi_{x-y}$  is above a certain threshold, the system forgets its state, resulting in a probability of flip of 1/2, while nothing occurs below the threshold. For higher temperatures, the probability of a spin flip becomes a smooth function of the contrast  $\psi_{x-y}$  (Fig. 2b). An unwanted side effect of the potential in Eq. 3 is that it couples the free and clamped sub-lattices. This is exemplified by the presence of Rabi oscillations between  $\psi_x$  and  $\psi_y$  when the potential coefficient  $\mu(t)$  is nonzero (Fig. 2c). However, the learning rule requires comparing two independent lattices. We mitigate this effect by keeping the

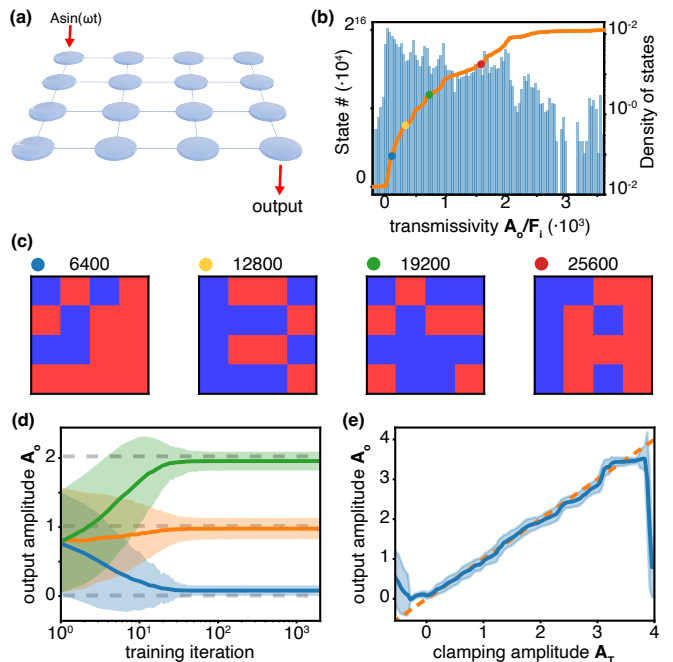


FIG. 3. Learning in a 4x4 lattice (a) System under consideration. A harmonic force with frequency  $\omega_c$  and amplitude  $F_i$  is applied at the top-left site, to both clamped and free degrees of freedom. The output amplitude  $A_o$  is measured at the bottom-right corner. (b) Cumulative density of states (orange) and density of states (blue) as a function of the transmissivity, computed via linearized model. The dots correspond to simulations of the transmissivity using the full nonlinear ODE with an excitation force of  $10^{-4}$ . (c) Spin textures corresponding to the dots in (b) (d) Evolution of the transmissivity as a function of training iteration for target values  $A_T$  of 0, 1 and 2 (dashed line). The line represents the mean of N simulations, while the shaded area represents a standard deviation. (e) Output amplitude  $A_o$  as a function of the clamping amplitude, after 200 learning iterations, starting from a random configuration. The shaded area represents one standard deviation. The dashed orange line corresponds to an ideal learning response. We observe that, for conductivity values for which spin state exists, the transmitted amplitude approximately converges to the clamping amplitude. Panels (d) and (e) are calculated with a sigmoidal flip probability ( $p_0 = 0$ ,  $\psi_T = 0.16$  and  $\beta = 1500$ ) and an input harmonic force  $F_i = 10^{-3}$ .

interaction strength to zero,  $\mu(t) = 0$ , during equilibration of the field  $\vec{\psi}$  in response to a change in the input. At every learning iteration, we apply the learning potential according to a Gaussian pulse, characterized by a peak value  $\mu_m$  and a width  $\Delta_t$ ,  $\mu(t) = \mu_m \exp\left\{-\frac{(t-t_0)^2}{2\Delta_t^2}\right\}$ . This potential causes the spins  $\sigma$  to be updated in response to the difference between clamped and free configurations. Since the decay rate of the the Ising mode  $\sigma_i$  is much faster than the decay rate associated with the computational modes  $\vec{\psi}_i$ , the contrast  $\psi_{x-y}$  remains significant during the learning iteration (Fig. 2c). Even if Rabi swaps occur between  $\psi_x$  and  $\psi_y$ , the contrast  $\psi_{x-y}$  is unaffected as  $H_L$  does not mix the  $\psi_{x+y}$  and  $\psi_{x-y}$

sectors.

Intuitively, we would expect the probability of spin-flip to follow a step-like change as a function of  $\psi_{x-y}$ : Below a critical detuning, the system remains in resonance and remembers its state, while above the threshold  $\psi_T$  the system falls out of resonance and forgets its state (Fig. 2a). At finite temperatures, this step-like response becomes a smooth sigmoidal function (Fig. 2b,d):

$$p(\psi_x - \psi_y) = p_0 + \frac{1}{4} [1 + \tanh(\beta(\psi_{x-y}^2 - \psi_T))], \quad (4)$$

in which the threshold  $\psi_T$  and the slope  $\beta$  are fitted empirically to a numerical simulation (Fig. 2d). Remarkably, the sigmoidal description breaks down for shorter pulse widths  $\Delta_t$ . In these cases, the oscillation of  $\sigma$  does not have time to decay below the thermal noise, thus forgetting its phase state (spin). In this short-pulse regime, the system presents coherent bit flipping—the spin changes deterministically for specific values of  $\psi_{x-y}$ —as opposed to conditional forgetting (Fig. 2d), which is the intended response.

## SITE-SITE INTERACTIONS

The interaction springs between computational degrees of freedom  $\vec{\psi}_i$  and  $\vec{\psi}_j$  are determined by the long term memory (weights) of the model, encoded in the spin texture of the  $\sigma$  field. In our model, this dependence arises through a nonlinear interaction  $H_I$  between each pair of nearest-neighbor sites  $i$  and  $j$ , with the form:

$$H_I = \lambda(t) [c_0 + (\sigma_i - \sigma_j)^2] \vec{\psi}_i^T \vec{\psi}_j, \quad (5)$$

This term induces an effective coupling spring  $c_{eff}$  between modes  $\psi_{x,i}$  and  $\psi_{x,j}$ , as well as between modes  $\psi_{y,i}$  and  $\psi_{y,j}$ ; with values  $c_{eff} = \lambda(t)c_0$  when the spins  $\sigma_i$  and  $\sigma_j$  are aligned, and  $c_{eff} = \lambda(t)(c_0 + 2A_\sigma^2)$  when  $\sigma_i$  and  $\sigma_j$  are anti-aligned (See Fig. 1 for a visual representation of this effect). Here,  $A_\sigma$  is the amplitude of oscillation of the Ising mode. During inference, the coupling strength  $\lambda(t)$  is set to a fixed value  $\lambda_0$ ; while at each training iteration it is momentarily set to 0 so that sites exactly follow the single-site learning dynamics described earlier. The term  $c_0$  ensures that there is some coupling even when the spins  $\sigma_i$  and  $\sigma_j$  are aligned—thus preventing a large number of spin configurations from collapsing to zero transmissivity. Although this work corresponds to a tight-binding model, in an experimental setting, the potential could be realized by a set of appropriately placed cubic springs (see Appendix C).

Due to the interaction term  $H_I$ , during inference ( $\lambda(t) = \lambda_0$  and  $\mu(t) = 0$ ), the dynamics of the  $\vec{\psi}$  field can be understood as a spin-dependent effective spring network, whose steady-state amplitude response is given by the linear system  $K(s)A_{\psi_{x/y}} = f_{\psi_{x/y}}$ . Here,  $K(s)$  is the spin-dependent stiffness matrix, whose diagonal components are  $K_{i,i} = i\omega_c^2/Q_c$  and the off-diagonal components

are given by  $K_{i,j} = -c_{eff}(s_i, s_j)$  when  $i$  and  $j$  are nearest neighbors, and zero otherwise. We choose  $\lambda_0$  and  $c_0$  so that the coupling stiffness is 10 times the damping rate  $\omega_c^2/Q_c$  for anti-aligned spins, and 2.5 times the damping rate for the aligned case. Here, we have introduced the variable  $s_i \in \{+1, -1\}$  to label the two possible phase oscillation states of  $\sigma_i$ . Gauge freedom means that the specific labeling is irrelevant as long as it is consistent between sites. We use this linearized model to study the expressivity of a square lattice with  $4 \times 4$  sites (Fig. 3a)—which output amplitude responses  $A_o$  can be encoded as a spin configuration  $s$ . We do so by computing the transmitted amplitude associated with every spin configuration and calculating an effective density of states (Fig. 3b,c). We observe that the lattice can encode a range of mostly positive transmissivities, with two small gap regions (Fig. 3b).

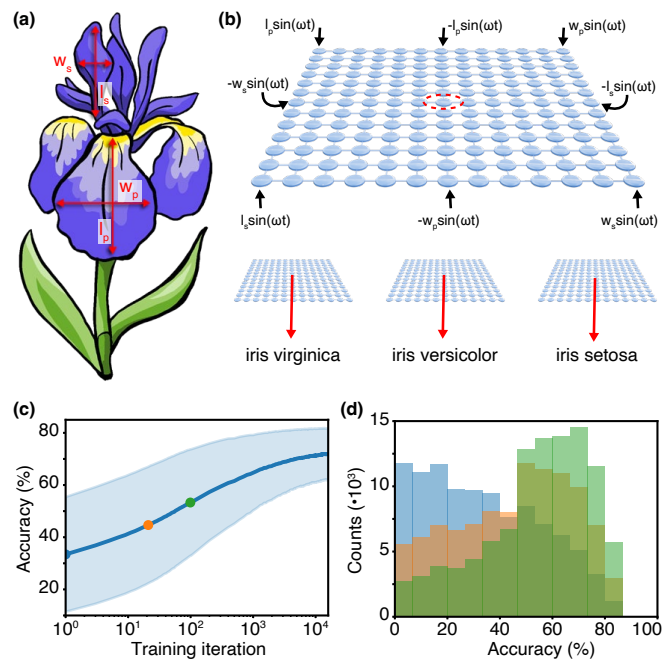


FIG. 4. Iris flower classification using a multifield coherent Ising machine. **(a)** The Iris dataset consists of the petal length  $l_p$ , petal width  $w_p$ , sepal length  $l_s$  and sepal width  $w_s$  for 150 flowers belonging to three classes (iris setosa, iris virginica, iris versicolor). **(b)** The features are injected into the multifield coherent Ising machine, by encoding them in the amplitude of harmonic excitations at the computational frequency  $\omega_c$ . The output is taken at the central site. Positive and negative copies of the signals are applied, as the lattice cannot perform subtractions. The full model consists of three multifield Coherent Ising Machines, corresponding to each of the model classes. The machines learn to produce a high amplitude when excited by a sample of their corresponding class. **(c)** Evolution of the mean classification accuracy during training. The shaded area corresponds to one standard deviation. **(d)** Histograms of the classification accuracy computed on an untrained lattice (blue), and after 20 (orange) and 98 (green) training iterations. The training times corresponding to the histograms are indicated as solid dots in panel (c).

Our lattice model can learn to approximate a given transmission amplitude (Fig. 3d, e), as long as the target amplitude can be expressed by a spin configuration. The learning protocol is as follows: We apply a harmonic force with magnitude  $F_i$  and frequency  $\omega_i$  at both clamped  $\psi_x$  and free  $\psi_y$  degrees of freedom of the the top-left site, while prescribing the displacement of the clamped mode  $\psi_y$  at bottom-right site to a target value  $A_T$ . During this procedure, we keep  $\lambda(t) = \lambda_0$  and  $\mu(t) = 0$ , waiting for a sufficient time ( $\Delta T \gg Q_c/\omega_c$ ) so that the  $\vec{\psi}$  field equilibrates. Then, we set  $\lambda(t) = 0$  and apply a Gaussian learning pulse  $\mu(t)$  to every site—during this protocol, the contrast  $\psi_{x-y}$  remains large owing to the long lifetime of the computational modes. For every target output amplitude  $A_T$ , we repeat this procedure  $n$  times, starting from a random spin configuration.

## LEARNING THE IRIS DATASET

We illustrate the capabilities of the proposed system on the Iris classification test [30]. The dataset consists of measurements of the petal length  $l_p$ , petal width  $w_p$ , sepal length  $l_s$  and sepal width  $s_w$  (Fig. 4a) for a set of 150 flowers belonging to the species *iris setosa*, *iris virginica*, and *iris versicolor*. The classifier consists of a system of three 13x13 lattices with one-hot encoding; the lattice with the highest output amplitude, measured at the central site, will be the inferred flower species. We apply the geometric features  $(l_p, w_p, l_s, w_s)$  by encoding them in the amplitudes of a set harmonic excitation forces at the frequency of the computational modes. These signals are applied at sites through the boundary of the lattice (Fig. 4b), acting on both free  $\psi_x$  and clamped  $\psi_y$  computational modes. Since the lattices cannot produce large negative transmissivities (Fig. 3b), we apply both positive and negative copies of each feature signal.

The training starts from three lattices with random spin configurations. Then, we apply the forces encoding

the features corresponding to a randomly chosen flower to each of the three lattices. We set  $\lambda = \lambda_0$  and  $\mu = 0$ , and clamp the output site  $\psi_{y,center}$  to 55 for the lattice corresponding to the current type of flower, and to  $-35$  for the lattices corresponding to the other flowers. Then, we apply a learning protocol to all lattices, consisting of setting  $\lambda = 0$  and  $\mu(t)$  to a Gaussian pulse, inducing bit flips when clamped and free sectors disagree. We simulate the training protocol by computing the steady-state amplitudes using the linearized model, and then flipping the bits with probabilities given by Eq. 4 with  $\alpha = 10$  and  $\psi_T = 1.5$ . We repeat this training for 2000 iterations, observing that the system starts from an accuracy of  $33.2 \pm 22.1\%$ , as one would expect from random choice. As more training iterations are performed—each consisting of a single, randomly-selected flower sample, the accuracy increases to  $71.9 \pm 9.8\%$ , more than halving the error rate, and significantly outperforming random choice. While this accuracy is lower than prior works on physical learning, we use a much simpler training method and network architecture. We expect that complex hierarchical networks trained with complex protocols should be able to reach performances comparable with the state-of-the-art.

## ACKNOWLEDGMENTS

We are thankful to Menachem Stern, Hermen-Jan Hupkes, Cyrill Bösch, Henrik Wolf, Tena Dubček and Martin van Hecke for helpful discussions. The illustrations in Fig. 1, 3a and 4a,b have been provided by Laura Canil from Canil Visuals. Funded by the European Union. Views and opinions expressed are however those of the author(s) only and do not necessarily reflect those of the European Union or the European Research Council Executive Agency. Neither the European Union nor the granting authority can be held responsible for them. This work is supported by ERC grant 101040117 (INFOPASS).

- 
- [1] H. Jaeger, B. Noheda, and W. G. Van Der Wiel, Toward a formal theory for computing machines made out of whatever physics offers, *Nature communications* **14**, 4911 (2023).
  - [2] F. Ashtiani, A. J. Geers, and F. Aflatouni, An on-chip photonic deep neural network for image classification, *Nature* **606**, 501 (2022).
  - [3] P. L. McMahon, The physics of optical computing, *Nature Reviews Physics* **5**, 717 (2023).
  - [4] A. Cordaro, H. Kwon, D. Sounas, A. F. Koenderink, A. Alù, and A. Polman, High-index dielectric metasurfaces performing mathematical operations, *Nano letters* **19**, 8418 (2019).
  - [5] S. Abdollahramezani, A. Chizari, A. E. Dorche, M. V. Jamali, and J. A. Salehi, Dielectric metasurfaces solve differential and integro-differential equations, *Optics letters* **42**, 1197 (2017).
  - [6] M. Aifer, K. Donatella, M. H. Gordon, S. Duffield, T. Ahle, D. Simpson, G. Crooks, and P. J. Coles, Thermodynamic linear algebra, *npj Unconventional Computing* **1**, 13 (2024).
  - [7] M. Aifer, S. Duffield, K. Donatella, D. Melanson, P. Klett, Z. Belateche, G. Crooks, A. J. Martinez, and P. J. Coles, Thermodynamic bayesian inference, *arXiv preprint arXiv:2410.01793* (2024).
  - [8] C. Turck, K.-E. Harabi, A. Pontlevy, T. Ballet, T. Hirtzlin, E. Vianello, R. Laurent, J. Droulez, P. Bessière, M. Bocquet, *et al.*, The logarithmic memristor-based bayesian machine, *arXiv preprint arXiv:2406.03492* (2024).
  - [9] F. Zangeneh-Nejad and R. Fleury, Topological analog signal processing, *Nature communications* **10**, 2058 (2019).

- [10] Z. Xue, T. Zhou, Z. Xu, S. Yu, Q. Dai, and L. Fang, Fully forward mode training for optical neural networks, *Nature* **632**, 280 (2024).
- [11] C. C. Wanjura and F. Marquardt, Fully nonlinear neuromorphic computing with linear wave scattering, *Nature Physics* **20**, 1434 (2024).
- [12] F. Zangeneh-Nejad, D. L. Sounas, A. Alù, and R. Fleury, Analogue computing with metamaterials, *Nature Reviews Materials* **6**, 207 (2021).
- [13] T. Dubček, D. Moreno-Garcia, T. Haag, P. Omidvar, H. R. Thomsen, T. S. Becker, L. Gebraad, C. Bärlocher, F. Andersson, S. D. Huber, *et al.*, In-sensor passive speech classification with phononic metamaterials, *Advanced Functional Materials* **34**, 2311877 (2024).
- [14] L. J. Kwakernaak and M. van Hecke, Counting and sequential information processing in mechanical metamaterials, *Phys. Rev. Lett.* **130**, 268204 (2023).
- [15] M. Cianchetti, M. Follador, B. Mazzolai, P. Dario, and C. Laschi, Design and development of a soft robotic octopus arm exploiting embodied intelligence, in *2012 IEEE International Conference on Robotics and Automation (IEEE, 2012)* pp. 5271–5276.
- [16] M. Stern and A. Murugan, Learning without neurons in physical systems, *Annual review of condensed matter physics* **14**, 417 (2023).
- [17] B. Scellier, A deep learning theory for neural networks grounded in physics, arXiv preprint arXiv:2103.09985 (2021).
- [18] B. Scellier and Y. Bengio, Equilibrium propagation: Bridging the gap between energy-based models and backpropagation, *Frontiers in computational neuroscience* **11**, 24 (2017).
- [19] M. Stern, D. Hexner, J. W. Rocks, and A. J. Liu, Supervised learning in physical networks: From machine learning to learning machines, *Physical Review X* **11**, 021045 (2021).
- [20] V. López-Pastor and F. Marquardt, Self-learning machines based on hamiltonian echo backpropagation, *Phys. Rev. X* **13**, 031020 (2023).
- [21] P. Milner, A brief history of the hebbian learning rule, *Canadian psychology = Psychologie canadienne* **44**, 5 (2003).
- [22] V. R. Anisetti, A. Kandala, B. Scellier, and J. Schwarz, Frequency propagation: Multimechanism learning in nonlinear physical networks, *Neural Computation* **36**, 596 (2024).
- [23] V. R. Anisetti, B. Scellier, and J. M. Schwarz, Learning by non-interfering feedback chemical signaling in physical networks, *Physical Review Research* **5**, 023024 (2023).
- [24] S. Dillavou, M. Stern, A. J. Liu, and D. J. Durian, Demonstration of decentralized physics-driven learning, *Physical review applied* **18** (2022).
- [25] S. Dillavou, B. D. Beyer, M. Stern, A. J. Liu, M. Z. Miskin, and D. J. Durian, Machine learning without a processor: Emergent learning in a nonlinear analog network, *Proceedings of the National Academy of Sciences* **121**, e2319718121 (2024).
- [26] C. Arinze, M. Stern, S. R. Nagel, and A. Murugan, Learning to self-fold at a bifurcation, *Physical Review E* **107**, 025001 (2023).
- [27] T. Inagaki, Y. Haribara, K. Igarashi, T. Sonobe, S. Tamate, T. Honjo, A. Marandi, P. L. McMahon, T. Umeki, K. Enbutsu, *et al.*, A coherent ising machine for 2000-node optimization problems, *Science* **354**, 603 (2016).
- [28] T. L. Heugel, O. Zilberberg, C. Marty, R. Chitra, and A. Eichler, Ising machines with strong bilinear coupling, *Phys. Rev. Res.* **4**, 013149 (2022).
- [29] V. Peri, M. Serra-Garcia, R. Ilan, and S. D. Huber, Axial-field-induced chiral channels in an acoustic weyl system, *Nature Physics* **15**, 357 (2019).
- [30] R. A. Fisher, The use of multiple measurements in taxonomic problems, *Annals of eugenics* **7**, 179 (1936).
- [31] R. H. Rand, *Mathieu’s equation* (2016).
- [32] M. H. Holmes, *Introduction to Perturbation Methods*, second edition ed., *Texts in Applied Mathematics*, Vol. 20 (Springer New York, New York, NY) pp. 139 – 146.
- [33] W. A. Benalcazar, B. A. Bernevig, and T. L. Hughes, Quantized electric multipole insulators, *Science* **357**, 61 (2017).
- [34] M. Serra-Garcia, V. Peri, R. Süsstrunk, O. R. Bilal, T. Larsen, L. G. Villanueva, and S. D. Huber, Observation of a phononic quadrupole topological insulator, *Nature* **555**, 342 (2018).
- [35] C. W. Peterson, W. A. Benalcazar, T. L. Hughes, and G. Bahl, A quantized microwave quadrupole insulator with topologically protected corner states, *Nature* **555**, 346 (2018).
- [36] K. H. Matlack, M. Serra-Garcia, A. Palermo, S. D. Huber, and C. Daraio, Designing perturbative metamaterials from discrete models, *Nature materials* **17**, 323 (2018).

#### Appendix A: Determination of the parametric resonance regions

In section we discussed how detuning of the parametrically pumped Ising mode leads to conditional forgetting. Here, we provide an in-depth analysis of parametric resonance using a combination of Floquet theory and perturbation methods. Our main objectives are to derive the resonance curve shown in Fig. 2a and to show that detuning has the effect of shifting it. The relevant equation is that of the Ising mode (Eq. 2) without interactions and noise, which can be cast in the following form:

$$\ddot{x} + \mu\dot{x} + (\delta + \epsilon \sin(t))x + \gamma x^3 = 0, \quad (\text{A1})$$

where  $\delta$  represents the squared ratio between the mode’s natural frequency and the pumping frequency and  $\epsilon$  represents the driving amplitude. Resonance occurs because the pumping effectively serves as a negative damping. Growing oscillations are detuned by the Duffing term, restricting the steady state amplitude. So, for fixed damping  $\mu$ , the relevant parameters that control whether or not resonance occurs are  $\delta$  and  $\epsilon$ . To derive the resonance curve in the  $\delta - \epsilon$  plane we treat the damping and Duffing terms as small perturbations to the well-known and extensively studied *Mathieu equation*:

$$\ddot{x} + (\delta + \epsilon \sin(t))x = 0, \quad (\text{A2})$$

for which the resonance regions can be found using Floquet theory. They form tongues emanating from the points  $\delta = n^2/4$  along the  $\delta$ -axis in what is known as the

Ince-Strutt diagram [31]. For the purposes of this paper, we consider the resonance region around the so-called *parametric resonance condition*, which holds when the driving frequency is twice the mode's natural frequency, or equivalently when  $\delta = 1/4$ . We can use perturbation theory to find an approximate expression for this resonance curve in the case where  $\mu, \gamma > 0$ , following an approach adapted from [31] known as the *the method of multiple scales*. Firstly, we treat the pumping amplitude  $\epsilon$  as a small perturbation, and rescale  $\mu$  and  $\gamma$  to be of the same order,  $\mu =: \epsilon\tilde{\mu}$  and  $\gamma =: \epsilon\tilde{\gamma}$ . Next, we expand the resonance curve in powers of  $\epsilon$ ,  $\delta = 1/4 + \delta_1\epsilon + \dots$  and define two independent timescales; a fast one  $\xi := t$  and a slow one  $\eta := \epsilon t$ . Because the timescales are assumed to be independent, the full time derivative with respect to  $t$  splits into partial derivatives with respect to  $\xi$  and  $\eta$  as follows:

$$\frac{d}{dt} = \frac{\partial}{\partial \xi} + \epsilon \frac{\partial}{\partial \eta}$$

Substituting everything into Eq. A1 and ignoring terms of second order or higher in  $\epsilon$ , leaves us with:

$$\frac{\partial^2 x}{\partial \xi^2} + 2\epsilon \frac{\partial^2 x}{\partial \eta \partial \xi} + \epsilon \tilde{\mu} \frac{\partial x}{\partial \xi} + \left( \frac{1}{4} + \epsilon \delta_1 + \epsilon \sin(\xi) \right) x + \epsilon \tilde{\gamma} x^3 = O(\epsilon^2). \quad (\text{A3})$$

Expanding the solution  $x$  in powers of  $\epsilon$ ,  $x = x_0 + x_1\epsilon + \dots$  and collecting terms of like order yields the following two equations (one for the zeroth and one for the first order):

$$\frac{\partial^2 x_0}{\partial \xi^2} + \frac{1}{4} x_0 = 0 \quad (\text{A4})$$

$$\frac{\partial^2 x_1}{\partial \xi^2} + \frac{1}{4} x_1 = -2 \frac{\partial^2 x_0}{\partial \eta \partial \xi} - \tilde{\mu} \frac{\partial x_0}{\partial \xi} - \delta_1 x_0 - \sin(\xi) x_0 - \tilde{\gamma} x_0^3. \quad (\text{A5})$$

From which we find the general solution for the zeroth order:

$$x_0 = A(\eta) \cos\left(\frac{\xi}{2}\right) + B(\eta) \sin\left(\frac{\xi}{2}\right). \quad (\text{A6})$$

Substituting this in the equation for the first order, and collecting resonance terms on the right hand side we find:

$$\begin{aligned} \frac{\partial^2 x_1}{\partial \xi^2} + \frac{1}{4} x_1 = & \sin\left(\frac{\xi}{2}\right) \left( A' + A \frac{\tilde{\mu}}{2} - B \delta_1 \right) \\ & - \cos\left(\frac{\xi}{2}\right) \left( B' + B \frac{\tilde{\mu}}{2} + A \delta_1 \right) \\ & - \sin\left(\frac{\xi}{2}\right) \left( \frac{3}{4} \tilde{\gamma} B^3 + \frac{3}{4} \tilde{\gamma} A^2 B + \frac{1}{2} A \right) \\ & - \cos\left(\frac{\xi}{2}\right) \left( \frac{3}{4} \tilde{\gamma} A^3 + \frac{3}{4} \tilde{\gamma} A B^2 + \frac{1}{2} B \right) \\ & + \text{off-resonance terms.} \end{aligned}$$

The terms on the left hand side that are on resonance are known as *secular terms* [32], and they cause the first

order  $x_1$  to grow without bound. So, in order for the perturbation assumption to be valid, these terms need to vanish. Setting the coefficients of the secular terms to zero leaves us with the following equations describing the (slow) dynamics of the amplitude and phase modulating the (fast) zeroth order oscillations  $x_0$ :

$$\begin{aligned} \frac{dA}{d\eta} &= \frac{1}{2} A (1 - \tilde{\mu}) + \delta_1 B + \frac{3}{4} \tilde{\gamma} B (A^2 + B^2) \\ \frac{dB}{d\eta} &= -\frac{1}{2} B (1 + \tilde{\mu}) - \delta_1 A - \frac{3}{4} \tilde{\gamma} A (A^2 + B^2). \end{aligned}$$

Note that the amplitude of the zeroth order oscillations is given by the length of the vector  $(A, B)$ . So, when the origin of the dynamical system above is stable, small oscillations of the parametrically driven mode die out, and when it is unstable, small oscillations are amplified. Therefore, the parametric resonance curve is defined by the parameter values at which the linearized system transitions from having no eigenvalues with positive real part, to having at least one. The eigenvalues of the linearized system are given by:

$$\lambda_{\pm} = -\frac{\tilde{\mu}}{2} \pm \sqrt{\frac{1}{4} - \delta_1^2}.$$

From this we conclude that the origin transitions from unstable to asymptotically stable when  $\lambda_- = 0$ . With some rearrangements, substituting back in  $\delta$  and  $\mu = \tilde{\mu}/\epsilon$ , we find the following equation for the resonance curve in the  $\delta - \epsilon$  plane:

$$\left( \delta - \frac{1}{4} \right)^2 = \frac{1}{4} (\epsilon^2 - \mu^2).$$

Finally, we can re-dimensionalize the expression by introducing the driving frequency  $\omega_d$ , which in Eq. 2 is set to  $2\omega_l$  in accordance with the parametric resonance condition:

$$\alpha^2 = \frac{\omega_d^2}{\omega_l^2 Q_l^2} + \left( \frac{\omega_d^2}{2\omega_l^2} - 2 \right)^2.$$

This is the expression used to determine the region of self-resonance in Fig. 2.

## Appendix B: Numerical methods

We solve the stochastic differential equations (SDEs) using a Splitting Path Runge-Kutta solver (SPaRK), while for the deterministic simulations (four dots in Fig. 3b), we use a Dormand-Prince algorithm with order 7-8. Both solvers are implemented in Python using the DiffraX library. We choose a time step for a minimum resolution of 50 points per period of oscillation.

## 1. Simulation of the learning process

We simulate this process by computing the equilibrium amplitudes of  $\vec{\psi}$  using the linearized model, and then determining the flip probability using the single-site flip probability (Eq. 4)—which provides an exact result as we switch off the inter-site potential during coupling.

### Appendix C: Realization of the interaction potential with nonlinear springs

The spin-dependent part of potential from Eq. 5 can be approximated by a set of cubic springs, governed by the Hamiltonian:

$$H_{I,ij} = \lambda'(t) \sum \alpha_k d_{v_{k,i}-u_{k,j}}^4, \quad (\text{C1})$$

where  $d_{v_{k,i}-u_{k,j}} = v_{k,i} - u_{k,j}$  is a difference between the field value  $v_{k,i}$  at drum  $i$  and the field value  $u_{k,j}$  at drum  $j$ . Field values are defined as a linear combination of modes,  $v_{k,i} = \vec{\kappa}_k^T \cdot (\psi_{x,i}, \psi_{y,i}, \sigma_i)$  and  $u_{k,j} = \vec{\kappa}'_k \cdot (\psi_{x,j}, \psi_{y,j}, \sigma_j)$  respectively. The coefficients  $\vec{\kappa}_k$ ,  $\vec{\kappa}'_k$  and value  $\alpha_k$  have been calculated to induce a spin-dependent spring between sites, while compensating for spin-dependent local frequency shifts in the computational and long-term degrees of freedom. These coefficients are provided in Table I. Although our work concerns a tight-binding model, a potential experimental realization might involve a mechanical resonator network, where each of the coupling terms in Eq. 5 corresponds to a cubic spring connecting a point  $\vec{r}_{1,k}$  in resonator  $i$  where the tight-binding basis functions  $\phi_{\sigma/\psi_x/\psi_y}(\vec{r}_{1,k})$  take the values  $\kappa_{1/2/3,k}$  with a point  $\vec{r}_{2,k}$  of resonator  $j$  where the tight-binding eigenfunctions  $\phi_{\sigma/\psi_x/\psi_y}(\vec{r}_{1,k})$  take the value  $\kappa'_{1/2/3,k}$ .

$\alpha_k$	$\kappa_k$	$\kappa'_k$
1	(1, 0, 1)	(1, 0, 1)
1	(0, 1, 1)	(0, 1, 1)
-1	(1, 0, 1)	(0, 0, 1)
-1	(0, 0, 1)	(1, 0, 1)
-1	(0, 1, 1)	(0, 0, 1)
-1	(0, 0, 1)	(0, 1, 1)
2	(0, 0, 1)	(0, 0, 1)

TABLE I. Coefficients for the inter-site interaction potential.

Of the seven interaction potential terms in Table I, the first two introduce the spin-dependent inter-site interactions between modes  $\psi_x - \psi'_x$  and  $\psi_y - \psi'_y$  respectively; the next four terms compensate for spin-dependent changes in the natural frequency of the computational degrees of freedom, while the last term compensates for spin-dependent changes in the Ising degrees of freedom. These extra terms are required to cancel the contribution of cross-products in Eq. C1, that do not exist in Eq. C. Only the first two terms determine the flow of information, as they couple computational degrees of freedom between sites. In absence of the compensating terms, the system may still be capable of learning. However, in this case, the output phase becomes dependent on the spin texture, which complicates the learning process.

The values in Table I have been determined by expanding Eq. C1 and choosing the coefficients to cancel on-resonance terms other than those in Eq. 5.

We expect that these results will motivate experimental realizations of the model, for example in metamaterial or optomechanical systems, in the same way that the emergence of topological tight-binding Hamiltonians [33] motivated the realization of metamaterial topological insulators [34–36]. In addition, this work poses a broad spectrum of novel questions exploring the realization of alternative learning potentials, learning rules and network architectures; the study of systems with more than two memory scales; as well as of the kinetics of the learning process.